The Astrophysical Journal, 759:85 (13pp), 2012 November 10 doi:10.1088/0004-637X/759/2/85

STUDY OF THE THREE-DIMENSIONAL CORONAL MAGNETIC FIELD OF ACTIVE REGION 11117 AROUND THE TIME OF A CONFINED FLARE USING A DATA-DRIVEN CESE–MHD MODEL

Chaowei Jiang (江朝伟)[1], Xueshang Feng (冯学尚)[1], S. T. Wu (吴式灿)[2], and Qiang Hu (胡强)[2]
[1] SIGMA Weather Group, State Key Laboratory for Space Weather, Center for Space Science and Applied Research, Chinese Academy of Sciences, Beijing 100190, China; cwjiang@spaceweather.ac.cn, fengx@spaceweather.ac.cn
[2] Center for Space Plasma and Aeronomic Research, The University of Alabama in Huntsville, Huntsville, AL 35899, USA; wus@uah.edu, qh0001@uah.edu
Received 2012 July 11; accepted 2012 September 10; published 2012 October 19

ABSTRACT

We apply a data-driven magnetohydrodynamics (MHD) model to investigate the three-dimensional (3D) magnetic field of NOAA active region (AR) 11117 around the time of a C-class confined flare that occurred on 2010 October 25. The MHD model, based on the spacetime conservation-element and solution-element scheme, is designed to focus on the magnetic field evolution and to consider a simplified solar atomsphere with finite plasma β. Magnetic vector-field data derived from the observations at the photosphere is inputted directly to constrain the model. Assuming that the dynamic evolution of the coronal magnetic field can be approximated by successive equilibria, we solve a time sequence of MHD equilibria based on a set of vector magnetograms for AR 11117 taken by the Helioseismic and Magnetic Imager on board the *Solar Dynamic Observatory* around the time of the flare. The model qualitatively reproduces the basic structures of the 3D magnetic field, as supported by the visual similarity between the field lines and the coronal loops observed by the Atmospheric Imaging Assembly, which shows that the coronal field can indeed be well characterized by the MHD equilibrium in most cases. The magnetic configuration changes very little during the studied time interval of 2 hr. A topological analysis reveals that the small flare is correlated with a bald patch (BP, where the magnetic field is tangent to the photosphere), suggesting that the energy release of the flare can be understood by magnetic reconnection associated with the BP separatrices. The total magnetic flux and energy keep increasing slightly in spite of the flare, while the computed magnetic free energy drops during the flare by $\sim 10^{30}$ erg, which seems to be adequate in providing the energy budget of a minor C-class confined flare.

Key words: magnetic fields – magnetohydrodynamics (MHD) – methods: numerical – Sun: corona

Online-only material: color figures

1. INTRODUCTION

Magnetic fields hold a central position in solar research, such as sunspots, coronal loops, prominences, and spectacular solar phenomena like flares and coronal mass ejections (CMEs). It has been commonly accepted that the energy released by a solar flare (which is usually up to the order of 10^{32} erg during major events) must be sourced from the magnetic field of an active region since all other possible energy sources are completely inadequate (Priest 1987). To help quantitatively understand solar explosive phenomena, such as flares and CMEs, it is essential to determine the amount of free magnetic energy and its temporal variation during the events. Most flare models consider magnetic reconnections as the basic mechanism for rapid energy conversion from the magnetic field into the kinetic and thermal counterparts (Priest & Forbes 2002; Shibata & Magara 2011). To locate where magnetic reconnection is prone to occur and produce a flare, one needs the three-dimensional (3D) coronal magnetic field, by which the important topological and geometrical features that are favorable sites for reconnection, e.g., the null point, the separatrices, or more commonly the quasi-separatrix layers (QSLs; Priest & Forbes 2002; Titov et al. 2002; Longcope 2005), can then be found. Unfortunately, the 3D magnetic field in the corona is very difficult to observe directly, although information about the field lines' 3D geometrical configuration can be partially reconstructed by the stereoscopy method, which uses coronal loops observed in different aspect angles in the EUV and X-ray wavelengths (see living review by Aschwanden 2011). Until now, a routinely direct and reliable measurement of the solar magnetic field was mainly restricted primarily to the solar surface, i.e., the photosphere (there are only a few cases available with the measurements of the chromospheric and coronal fields, e.g., Solanki et al. 2003; Lin et al. 2004).

With the observed magnetic field on the photosphere in hand, there are several ways to study the evolution of the 3D magnetic field in the corona. One of them is a well-known model of field extrapolation from the magnetogram, specifically a nonlinear force-free (NLFF) field extrapolation (Wiegelmann 2008; Schrijver et al. 2008; DeRosa et al. 2009). As the solar corona is dominated by the magnetic field environment with very small plasma β (the ratio of gas pressure to magnetic pressure), the force-free model is usually valid and serves as a good approximation for the low corona (but above the photosphere) in a near-static state. A variety of numerical codes have been developed to implement the force-free field extrapolation in the past decade (e.g., Wheatland et al. 2000; Wiegelmann 2004; Amari et al. 2006; Jiang & Feng 2012). These methods have been successfully applied in analyzing the magnetic structures of active regions, the electric current distributions, the energy budget of eruptions, etc. (Régnier & Canfield 2006; Guo et al. 2008; Thalmann & Wiegelmann 2008; Jing et al. 2010; Valori et al. 2012; Sun et al. 2012), such as reproducing field lines comparable to observed coronal loops (e.g., Wiegelmann et al. 2012) and extrapolating complex flux rope, which is believed to be associated with the filament channel (e.g., Canou & Amari 2010). However, it should be noted that success is still limited when applied to realistic solar data (Schrijver et al. 2008; DeRosa et al. 2009; Schrijver 2009), primarily because of the intrinsic non-force-freeness in the field close to the photosphere

(Metcalf et al. 1995). Thus, the observed data does not generally provide a consistent boundary condition for the model based on an exact force-free assumption, and some ad hoc preprocessing (to *remove* the force in the raw magnetogram) is usually done to prepare the vector magnetograms for the extrapolation codes (Wiegelmann et al. 2006).

Another method is using a data-driven magnetohydrodynamics (MHD) model, which is more general than the force-free one (Wu et al. 2006, 2009; Wang et al. 2008; Jiang et al. 2010; Fan et al. 2011, 2012). This is because in the MHD model, nonlinear dynamic interactions of the magnetic field and plasma flow field are treated in a self-consistent way in which the near force-free state of the coronal magnetic field is included. A data-driven MHD model was first developed by Wu et al. (2006) for simulating the evolution of active regions. In their original work, the initial setup of the model is established by seeking an MHD equilibrium started from an arbitrarily prescribed plasma and a potential magnetic field based on the *Solar and Heliospheric Observatory* (*SOHO*)/MDI magnetogram at a given time. Then a time series of MDI magnetograms observed afterward were continuously inputted at the bottom boundary to drive the above field to respond to the changes in the photosphere. In particular, the procedure of continuously feeding observed data into the bottom boundary is made to be self-consistent by a projected-characteristic method (e.g., Nakagawa 1981; Wu & Wang 1987).

If under an ideal or strict condition, this dynamic process of the data-driven model can indeed be regarded as evolution of the corona. However, in reality, there are still many difficulties and problems in using a data-driven MHD model to study active region evolution. First of all, there is a lack of observations of the photospheric parameters of plasma, such as the surface flow velocity, which is important boundary information for the driving process (Abbett et al. 2004; Welsch et al. 2004). This is especially essential since the magnetic field may be dominated by dense plasma (with a high β) in the photosphere, and field lines anchored in the photosphere can usually be considered as line tied by the photospheric plasma because of the high electric conductivity (Priest 1987; Mikic & Linker 1994; Solanki et al. 2006). This means that field-line footpoints are passively advected by the plasma flow, which itself is induced in the convection zone below. Without surface flow information, the response of the coronal field lines, driven by the photospheric footpoint motion, cannot be fully followed. This encourages people to recover the photospheric flow velocity from the time-varying magnetograms by using a local correlation tracking technique or similar methods (e.g., see Chae 2001; Welsch et al. 2004; Démoulin & Pariat 2009). The second problem comes from the cadence of the observed data, which is generally too low for a data-driven model that needs a highly continuous data flow. To address this problem, Wu et al. (2006) simply used a time-linear interpolation on the 96 minute cadence MDI magnetograms to provide the data needed at each time step (about 6 s used by Wu et al. 2006) of the model. This obviously oversimplifies the real evolution of the photospheric field, which is very time nonlinear, but it may be the only choice one can make.[3] In view of these two problems, it may be more practical to construct independent MHD equilibria for each of the magnetograms and consider these successive equilibria as the continuous time evolution of the corona, as done by Wu et al. (2009) and Fan et al. (2011).

[3] This problem can now be alleviated using recently available data recorded by HMI on board the new observatory *SDO*, which has a higher data cadence.

For the third problem, it is difficult to couple the photospheric and coronal plasma into a single model because of the highly stratified plasma, of which the parameters, i.e., the density and the temperature, change drastically by several orders of magnitude within an extremely thin layer (the chromosphere and transition region) above the photosphere due to some kind of unknown coronal heating process. For a realistic model with inputted magnetic field data observed in the photosphere, it is required to describe the behavior of the magnetic field in this stratified environment with plasma β varying from >1 (the photosphere) to $\ll 1$ (the corona). However, this greatly challenges the numerical scheme and computational resource to treat the transition region. Additionally, one may need to incorporate the complicated thermodynamic processes of the real corona, such as thermal conduction and radiative losses (e.g., see models by Abbett 2007; Fang et al. 2010). We note that in the works of Wu et al. (2006, 2009), Wang et al. (2008), and Fan et al. (2011), only the photospheric or near-photosphere plasma is considered in the models, and thus these models are mainly used for studying the evolution of photospheric parameters, such as the plasma flow, the Poynting flux, the current helicity, and some other non-potential parameters at the photosphere level. The evolution of the 3D coronal magnetic field, on the other hand, was rarely studied using these models because of the unjustified high-β and dense plasma environment. This is due to the reason mentioned above where a coupled modeling of the photospheric and coronal fields is still computationally prohibitive.

In this work, we will use the data-driven MHD model to study the 3D coronal field within a low plasma-β condition. The numerical model is developed following our previous work (Jiang et al. 2011), which has been devoted to a validation of the conservation-element and solution-element (CESE) MHD method for reconstructing the 3D coronal fields using a semi-analytic force-free field solution proposed by Low & Lou (1990). We will study the 3D magnetic field and its evolution in active region NOAA AR 11117 around the time of a small C-class flare that occurred on 2010 October 25, observed by the *Solar Dynamic Observatory* (*SDO*) Atmospheric Imaging Assembly (AIA) with a time series of vector magnetograms recorded by *SDO* Helioseismic and Magnetic Imager (HMI). While the 3D magnetic field of the same active region has been studied by Sun et al. (2010) and Tadesse et al. (2012) using the NLFFF model, this is the first study where we apply the CESE–MHD model to realistic solar data. Similarly, assuming that the evolution of the coronal magnetic field in the active region can be described by successive equilibria (e.g., Régnier & Canfield 2006; Wu et al. 2009; Sun et al. 2012; Tadesse et al. 2012), we use each vector magnetogram of the data set to get a snapshot MHD equilibrium and study the temporal evolution of the field by a series of these equilibria. This method is justified by considering that the evolution of the active region, driven by the photospheric motion with a flow speed on the order of several km s^{-1}, is sufficiently slow compared to the speed to the coronal magnetic field relaxing to equilibrium, which is up to thousands of km s^{-1} (Antiochos 1987; Seehafer 1994). It is also valid for the present studied objective, AR 11117, which shows no major changes in the magnetic field in the chosen time period.

The remainder of the paper is organized as follows. In Section 2, we give a brief description of the CESE–MHD model. Magnetic field data used to drive the model are described in Section 3. The modeling result for AR 11117 is presented in Section 4, including a qualitative inspection of the 3D magnetic

configurations, topological analysis of the field at the flare site, as well as a study of the magnetic energy budget and current distribution. Finally, we draw conclusions and give some outlooks for future work in Section 5.

2. THE DATA-DRIVEN CESE–MHD MODEL

In a nutshell, we intend to solve a set of MHD equilibria, each of which is consistent with a snapshot of the magnetic field observed in the photosphere. We thus start from an arbitrarily initial field, e.g., a potential or linear force-free field, with a plasma and input at the bottom of the model, the vector magnetogram, to drive the system away from its initial state and then let the system relax to a new equilibrium. The numerical model follows our previous work (Jiang et al. 2011). Since the computation is focused on the magnetic field and its dynamics with plasma in the low corona, here we use a simplified solar atmosphere with a low plasma β and a uniform constant temperature. Thus, the numerical scheme need only handle the plasma density ρ, the flow velocity $\mathbf{v}$, and the magnetic field $\mathbf{B}$. The MHD equations are written as follows:

$$\begin{aligned}\frac{\partial \rho}{\partial t} + \nabla \cdot (\rho \mathbf{v}) &= 0,\\ \rho \frac{D\mathbf{v}}{Dt} &= -\nabla p + \mathbf{J} \times \mathbf{B} + \rho \mathbf{g} + \nabla \cdot (\nu \rho \nabla \mathbf{v}) - \nu_f \rho \mathbf{v},\\ \frac{\partial \mathbf{B}}{\partial t} &= \nabla \times (\mathbf{v} \times \mathbf{B}). \end{aligned} \quad (1)$$

In these equations: $\mathbf{J}$ is the electric current; p is the gas pressure given by $p = \rho R T_0$, where R is the gas constant and T_0 is the constant temperature; and $\mathbf{g}$ is the solar gravity and is assumed to have a constant photospheric value since we simulate the low corona with a height of about 100 Mm from the photosphere. A small kinematic viscosity ν with a value of $\sim \Delta x^2/\Delta t$ ($\Delta x, \Delta t$ are respectively the grid spacing and the time step in the numerical scheme) is added for numerical stability.

We use equations different from Jiang et al. (2011). Here we include an additional frictional force $-\nu_f \rho \mathbf{v}$ to address the problem where, in some odd places near the magnetogram (i.e., the bottom), the plasma velocity is prone to be accelerated to extremely high values due to very large gradients or some kind of uncertainties intrinsically contained in the observed data. This is because the data are very intermittent in the observed magnetograms, which usually show a large number of small-scale polarities and even apparent discontinuities, and these features cannot be adequately resolved by the grid resolution. We find that such problems can severely restrict the time step and slow the relaxation process of the entire system, even making the computation unmanageable. It should be noted that including the friction force is only an ad hoc choice for numerical consideration when dealing with the original data in the model. Alternatively, one can smooth the original magnetograms beforehand to remove noise and decrease large gradients in the raw data. This, however, may erase some important parasitic polarities around the major sunspots and also probably change the locations of the polarity inversion lines (PILs), which could influence the analysis of the local field configurations responsible for small-scale energy dissipation near the photosphere (e.g., the small flare in the present study). Also there is magnetic flux loss and the energy content of the field may be affected if the vertical component of the magnetogram is modified (Metcalf et al. 2008). Although the field at the coronal base ought to be smoother than the photospheric field because of the field expansion from the high-β to the low-β regions, the way in which such smoothness can be modeled is still problematic. To this end, it is prudent not to smooth the original magnetograms, and thus we use the frictional force to control the above-mentioned problem in the numerical computation. We have tried different values for the frictional coefficient ν_f and adopt an optimized one, $\nu_f = 1/(50\Delta t)$, which can control the plasma flow to a reasonable level, i.e., the flow speed is suppressed under the maximum Alfvén speed but not too much. Our tests show that the adjustment of ν_f affects the MHD relaxation process but gives almost the same final solution. Finally, no explicit resistivity is included in the magnetic induction equation, since the numerical diffusion can lead to topological changes of the field when necessary.

The above equation (1) is solved by our CESE–MHD code (Jiang et al. 2010). The CESE method deals with the 3D governing equations in a substantially different way that is unlike traditional numerical methods (e.g., the finite-difference or finite-volume schemes). The key principle, which is also a conceptual leap of the CESE method, is treating space and time as one entity. By introducing the conservation-element (CE) and the solution-element (SE) as the vehicles for calculating the spacetime flux, the CESE method can enforce conservation laws both locally and globally in their natural spacetime unity form. Compared with many other numerical schemes, the CESE method can achieve higher accuracy with the same mesh resolution and provide simple mathematics and coding free of any type of Riemann solver or eigendecomposition. For more detailed descriptions of the CESE method for MHD simulations including the multi-method control of the well-known $\nabla \cdot \mathbf{B}$ numerical errors, please refer to our previous work, e.g., Feng et al. (2006, 2007) and Jiang et al. (2010, 2011). We use a non-uniform grid within the framework of a block-structured, distributed-memory parallel computation. The grid configuration is depicted in Figure 1. Specifically, the whole computational volume is divided into blocks with different spatial resolutions, and the blocks are evenly distributed among the CPU processors. In the x–y plane, i.e., the plane parallel with the photosphere, the blocks have the same resolution. In the vertical direction, block resolutions decrease with height, e.g., near the photosphere the grid spacing matches the resolution of the magnetogram, and at the top of the model box the grid spacing increases four times. As shown in Figure 1, at a height of only 10 Mm the magnetic field has become far less intermittent, i.e., much smoother than at the photosphere. Thus, using this non-uniform mesh does not affect the computational accuracy much compared to a uniform mesh, but can save significant computational resources.

The initial configuration of the simulation consists of a potential field matching the vertical component of the magnetogram and a plasma in hydrostatic equilibrium in the solar gravitational field. The potential field is obtained by a Green's function method (e.g., Metcalf et al. 2008). The plasma density is given by $\rho(z) = \rho_0 \exp(-z/H)$, where H is the pressure scale height, $H = RT_0/g$, and $z = 0$ denotes the photosphere. Nondimensionalization of the parameters is the same as in Jiang et al. (2011), and Figure 2 shows a typical configuration of the parameters along a vertical line through the computation volume in the strong magnetic region. It is noteworthy that the plasma β can be large in the relatively weak field region, and thus the intrinsic force in the vector magnetogram can be self-consistently balanced by the plasma in the MHD relaxation process. This is unlike the force-free model, as aforementioned (see Section 1), which generally cannot deal with the observed data directly. The boundary conditions are also very similar to those used in Jiang

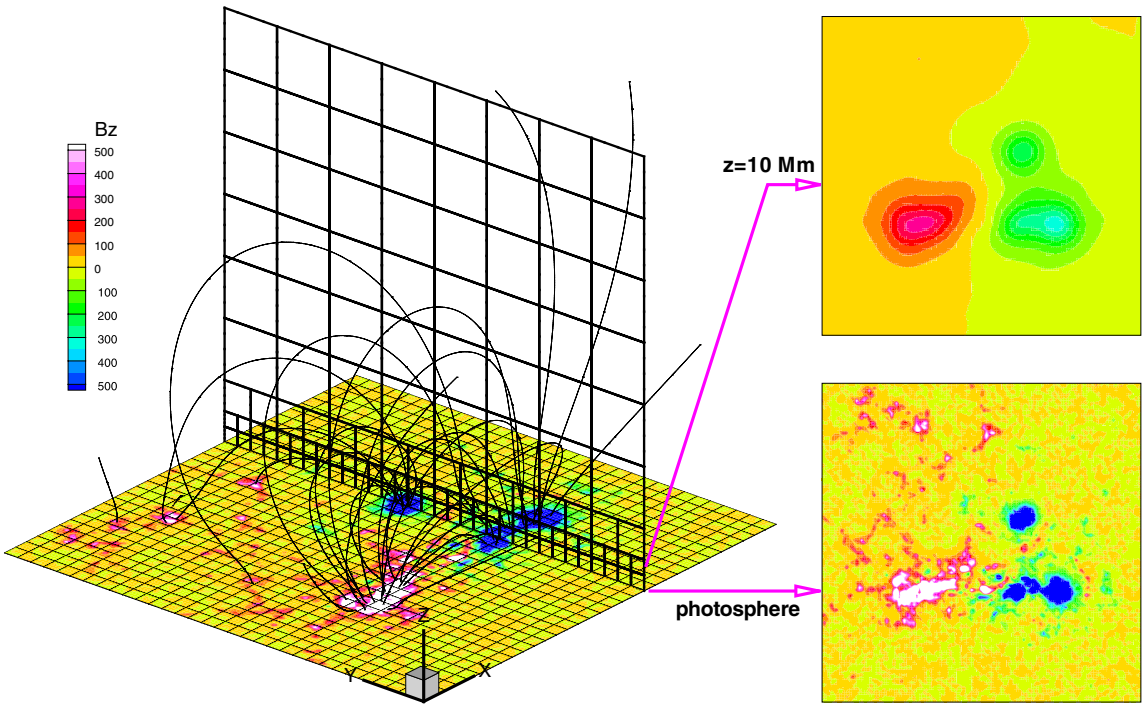

Figure 1. Configuration of the computational grid. The entire volume is divided into blocks and each block has 8 × 8 × 8 cells. In the left panel, two slices through the volume are plotted to show the structure of the blocks, which are outlined by the black grid lines; the bottom contour map represents B_z on the photosphere and the curved lines show the potential field lines. The right panels show the 2D contour images of B_z sliced at $z = 0$ and $z = 10$ Mm (locations in the 3D grid are shown by the arrows).

(A color version of this figure is available in the online journal.)

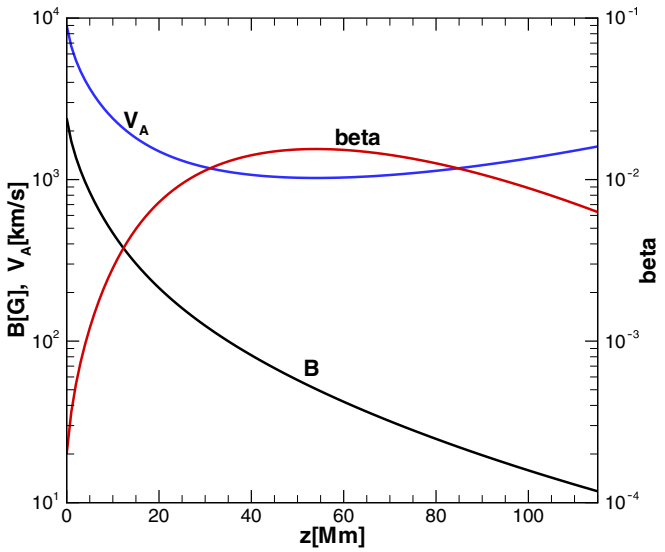

Figure 2. Typical configurations of the magnetic field strength B, the Alfvén speed V_A, and the plasma β along a vertical line through the computation volume.

(A color version of this figure is available in the online journal.)

et al. (2011): the bottom boundary is incrementally fed with the observed vector magnetogram in tens of Alfvén time until the observed data are fully matched, and all other boundaries are set by the non-reflecting boundary conditions. Besides, the flow velocity on the bottom is set by extrapolation from the neighboring inner grid. This has the function of increasing the communication between the magnetogram and the computational volume (Valori et al. 2007).

3. DATA

NOAA AR 11117 was observed by *SDO* from 2010 October 20 to 2010 November 2, mainly during Carrington Rotation 2102. On 2010 October 25, it was crossing the central meridian of the solar disk with a latitude of 22° as shown in the full-disk HMI and AIA images (Figure 3). On this date, solar activity was dominated by AR 11117 with several small B-class flares observed, and near the end of the day, a C2.3-class flare occurred. NOAA records indicate that the event began in soft X-rays, which were detected by the *GOES* (*Geostationary Operational Environmental Satellite*) 15 satellite at 22:06 UT, reaching a peak at 22:12 UT and ending at 22:18 UT (see Figure 4). As observed by AIA (see Figure 6), the central part of the active region shows distinct brightenings at the flare peak time, and the flare is confined to a rather low altitude without inducing major changes in the coronal loops or eruptions.

We select a set of vector magnetograms for AR 11117, which were taken by HMI around the flare peak time with a cadence of roughly half an hour. The data are de-rotated to the disk center, and the field vectors are transformed to Heliographic coordinates with the projection effect removed and finally remapped to a local Cartesian coordinate using Lambert equal area projection. For a detailed processing of the HMI vector magnetograms, please refer to http://jsoc.stanford.edu/jsocwiki/VectorMagneticField. Specifically, six magnetograms taken at 21:00, 21:36, 22:00, 22:12, 22:36, and 23:00 UT, respectively, are used for the simulation. Figure 5 shows examples of the vector magnetograms before and at the flare peak time (the gray image shows the vertical component B_z, and the arrows indicate the transverse field). There are four regions with flux greater than 1000 G concentrated in areas of about 10 arcsec^2, and these regions manifest as four main sunspots observed in the AIA 4500 Å (white light)

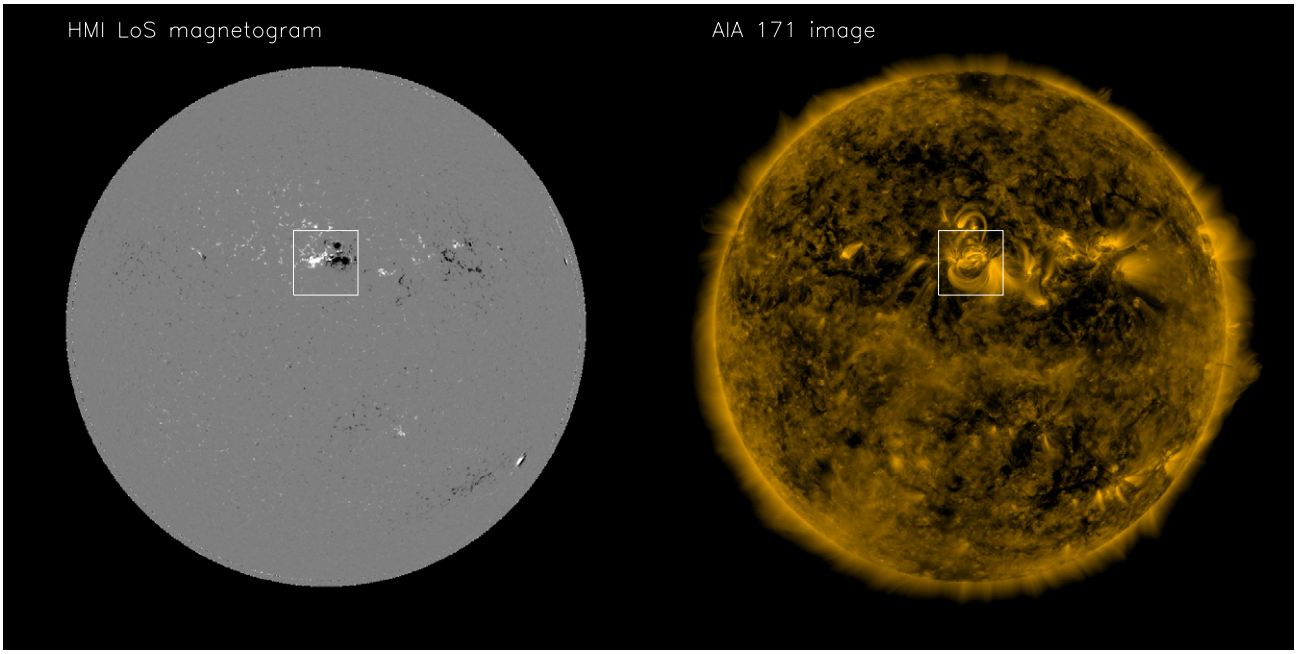

Figure 3. Full-disk *SDO*/HMI line-of-sight (LoS) magnetogram (left) and full-disk *SDO*/AIA 171 Å image. Both images were obtained at the same time, 22:12 UT on 2010 October 25, and have been co-aligned. AR 11117 is outlined by the white rectangle on the images.
(A color version of this figure is available in the online journal.)

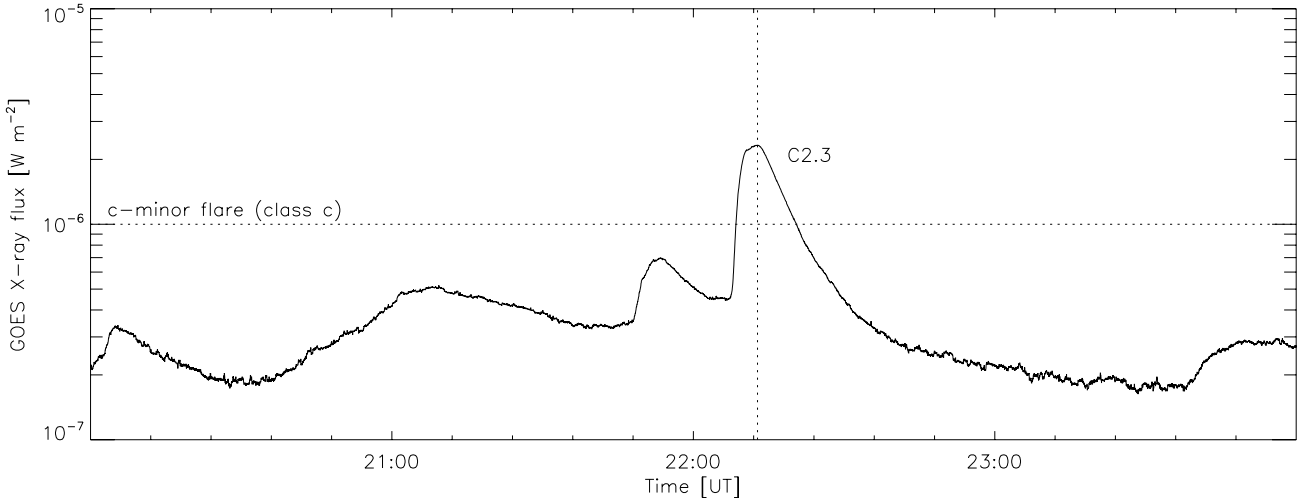

Figure 4. *GOES* soft-X ray flux from 20:00 UT to 24:00 UT on 2010 October 25 in the wavelength range of 1–8 Å. The horizontal dotted line indicates the C-minor flare class and the vertical dotted line indicates the peak time of the flux.

image. A strong shear of the transverse field can be seen near the image center, with the vector almost parallel to the PIL (see the regions where the color of the vectors changes while their directions are nearly the same). The original resolution of the magnetogram is about 0.5 arcsec pixel^{-1} (∼360 km), and we bin the data to 1 arcsec pixel^{-1} for our simulation with a field of view of 256 × 256 arcsec^2 (184 × 184 Mm^2). The height of the computational box is set to 160 arcsec (115 Mm). To reduce the side and top boundary influence, the following analysis of the results is performed on a sub-volume with $200 \times 128 \times 100$ arcsec^3 centered in the full computational domain.

4. RESULTS

4.1. Comparison with AIA Loops

The high-resolution coronal loops observed by *SDO*/AIA in the wavelength of 171 Å give us a proxy of the magnetic field line geometry (see the left column of Figure 6) and are also a good constraint for the magnetic field model. In the middle column of Figure 6, we show some selected magnetic field lines of the model results. In these images, the yellow lines represent the magnetic field lines and the background contours outline the vertical component of the magnetogram. For a visual comparison with the observed coronal loops, we plot the figures side-by-side with the AIA 171 Å images observed at the same time. The field lines are selected roughly according to the visible bright loops, and the angle of view of the MHD results is co-aligned with the AIA image. As shown from an overview of the figures, the simulated field lines closely resemble the observed loops, especially at the central region of the AR where the field lines are strongly sheared. This means that the field there is very non-potential. The potential fields at each time are shown in the third column of Figure 6. Compared to the potential field lines, the MHD field lines exhibit some twists,

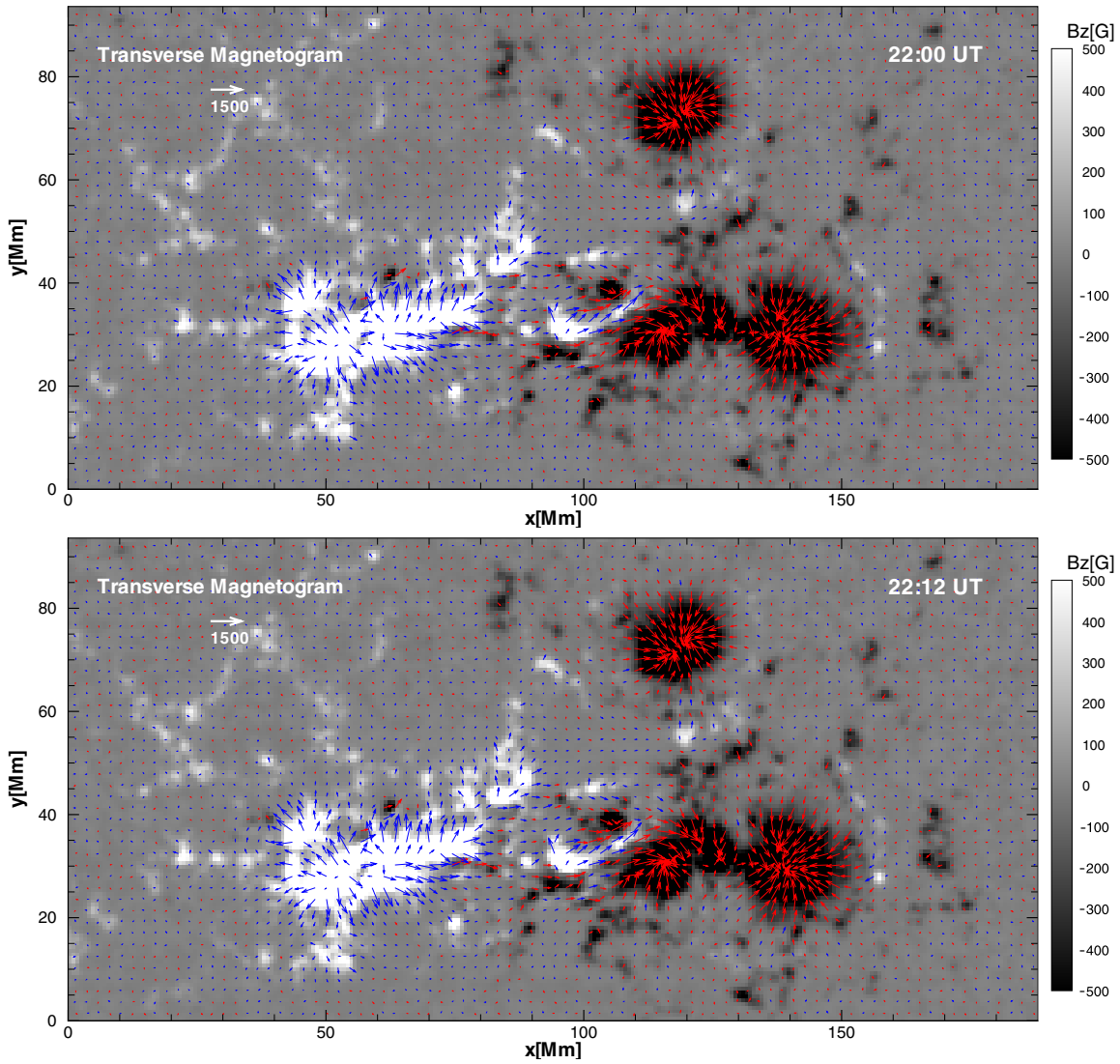

Figure 5. Vector magnetograms for AR 11117 at 22:00 and 22:12. The gray images represent B_z with a saturation level of ±500 G. The tangential fields are shown by the vectors (plotted at every third pixel point) with blue in the positive B_z region and red in the negative B_z region.

(A color version of this figure is available in the online journal.)

although they are not strong, implying the existence of field-line-aligned currents (i.e., currents along the field lines). We find that there are some features that are well reproduced by the MHD model, but they failed to be recovered by the potential model, e.g., the structures pointed out by the white arrows in the figure. Reconstruction of these features, which obviously need to have different field-line connectivities from those of the initial potential field, demonstrates that our model can indeed reconstruct the 3D magnetic topology that is implied in the observed transverse field.

By comparison, we conclude that within this AR, the MHD model gives much better results than the potential field model. Although some small changes can be recognized in the loops and the MHD field lines during this time interval, it is difficult to find any variation in the magnetic topology around the time of the flare from 22:00 to 22:12. This means that the flare-related reconnection takes place on a rather small scale and at a low height near the photosphere (as indicated by the analysis of magnetic topology in the following section). It can be clearly seen in the AIA image at 22:36 that there are two groups of loops that are much brighter than the other loops, and the MHD model appears to fail to reproduce the groups in the north (i.e., the loops pointed out by the black arrow in the image; note that this group of loops is difficult to find in all the other AIA images in the figure). This may be due to the fact that the central part of the active region is very dynamic after the flare since hot plasma from the chromosphere "evaporated" to the post-flare loops, and thus cannot be well described by the quasi-static state which we have sought.

4.2. Topological Analysis of the Flare Location

It has been thought that it is plausible for a flare to occur in regions with strong variation in field line connectivity (e.g., Mandrini et al. 1995; Demoulin et al. 1997). Such regions are called QSLs, which are generalized from the concept of magnetic separatrices where the field-line linkage (or connectivity) is discontinuous (Priest & Démoulin 1995; Demoulin et al. 1996). To locate QSLs in the 3D coronal field, Titov et al. (2002) introduced a so-called *squashing factor* (Q) to quantify the change of the field linkage based on field-line mapping. For the corona field, the mapping is defined by one photospheric footpoint (x, y) of a given field line to

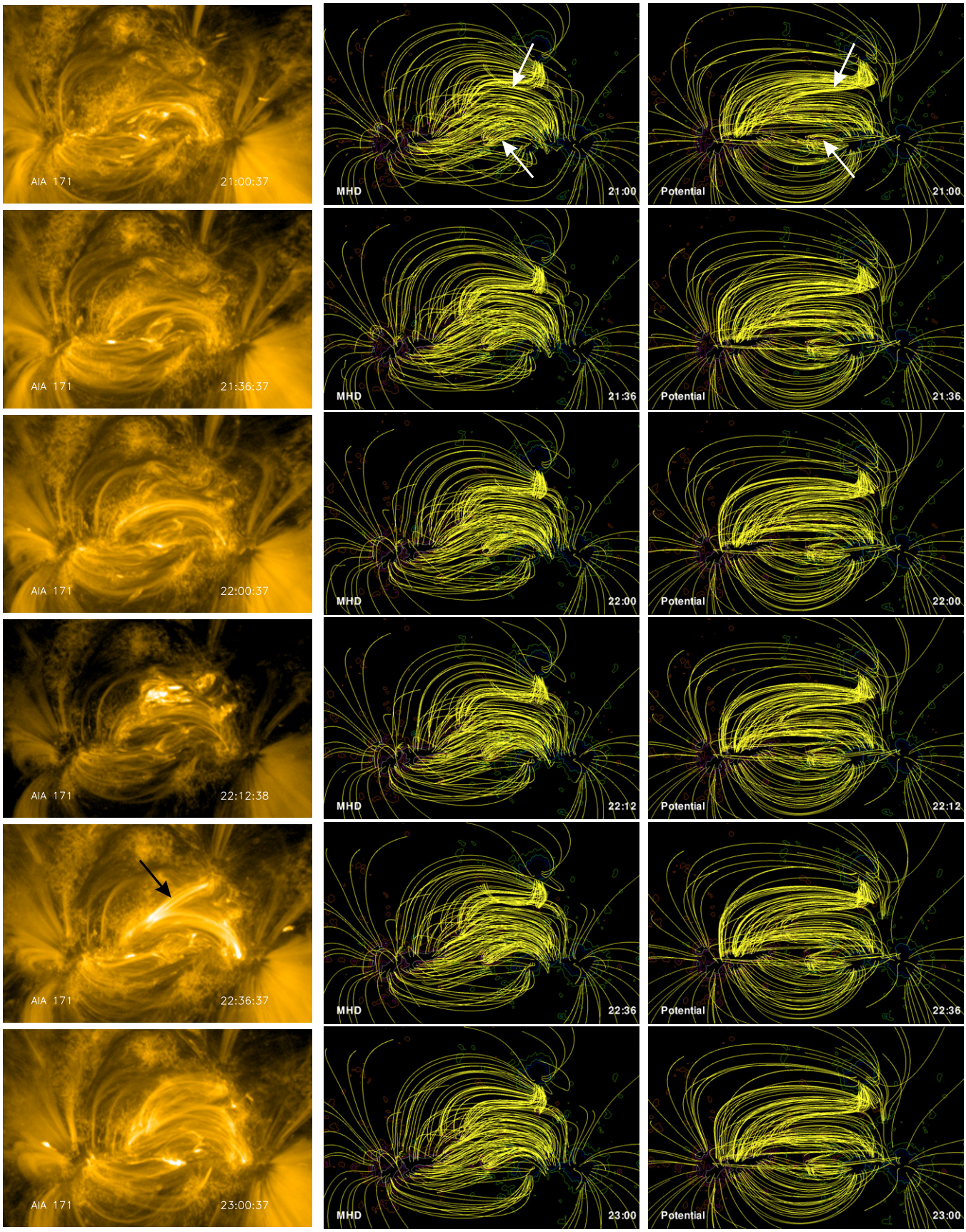

Figure 6. Comparison of the modeled field lines with the *SDO*/AIA 171 Å image for AR 11117. The left column is the AIA images, and the middle column is the selected magnetic field lines from the MHD results. Also the potential field lines are plotted in the last column. The field lines in all the panels are traced from the same footpoints on the photosphere, and the color contours of photospheric B_z are plotted on the background.

(A color version of this figure is available in the online journal.)

the other photospheric footpoint $(X(x, y), Y(x, y))$, which is also called the magnetically conjugate footpoint.[4] Then the squashing factor is given by

$$Q = \frac{a^2 + b^2 + c^2 + d^2}{|ad - bc|}, \tag{2}$$

where

$$a = \frac{\partial X}{\partial x}, \quad b = \frac{\partial X}{\partial y}, \quad c = \frac{\partial Y}{\partial x}, \quad d = \frac{\partial Y}{\partial y}. \tag{3}$$

Producing a map of the Q factor is a robust way of finding topological elements (including both the QSLs and the separatrices) in the 3D magnetic field, but its calculation is computationally intensive because field lines are required to be traced from not only each point, but also from its neighboring points to estimate the derivatives of the field line mapping. We thus use the following algorithm: first, a field line from each grid point (i, j) on the bottom surface is traced either forward or backward and the location of the other (conjugate) footpoint is denoted by $(X(i, j), Y(i, j))$; then at each grid point, a centered difference involving its neighboring four grid points $(i - 1, j), (i + 1, j), (i, j - 1), (i, j + 1)$ is used to approximate the elements needed by Q, i.e.,

$$\begin{aligned} a &= \frac{X(i+1, j) - X(i-1, j)}{2\Delta x}, \\ b &= \frac{X(i, j+1) - X(i, j-1)}{2\Delta y}, \\ c &= \frac{Y(i+1, j) - Y(i-1, j)}{2\Delta x}, \\ d &= \frac{Y(i, j+1) - Y(i, j-1)}{2\Delta y}, \end{aligned} \tag{4}$$

where Δx and Δy are the grid spacings. To avoid the numerical uncertainties of tracing field lines with very small structures near the photosphere (i.e., structures smaller than the grid resolution), we raise the bottom surface by three pixels (about 2 Mm) above the photosphere in the computation. This might smooth out some very fine structures in the Q map, but the basic topological features remain since they depend mainly on large-scale current distribution (Titov & Démoulin 1999). As suggested by Titov et al. (2002), it is also useful to compute the expansion-contraction degree (K), which is defined by the ratio of the normal components of the magnetic field at the two ends of the field lines. While the factor K has a similar function to Q in locating the QSLs, it is much simpler to compute than the latter and may be more reliable since its computation is free of the numerical errors of the finite difference in Equation (4).

Considering that the magnetic field is nearly steady with time, we only compute the QSLs for a single frame. Figure 7 depicts the Q and K maps (panel (b) and (d)) for the magnetic field at 22:12 and compares them to the AIA image at the same time. We use a logarithmic scale since the squashing factor abruptly becomes very large inside the QSLs (e.g., Titov et al. (2002) defined the QSL as a region with $Q \gg 2$). Note that there are data gaps in the maps because the field lines there are opened, i.e., with ends of the lines reaching the side or top boundaries of the computational volume. As shown by the Q and K maps, the structures associated with data abrupt change, i.e., the QSLs, are consistent between both maps. The whole structure of the Q map is rather complicated and may deserve a comprehensive study, while here we put our focus on analyzing the relation of the flare location (outlined by the dashed rectangle on the AIA image) with the QSLs. Indeed, the flare location is clearly co-spatial with the QSL, where the squashing factor reaches $\sim 10^3$ (see the region in the dashed rectangle on the Q map). Then why does this subregion have a strong change of magnetic connectivity? In the same figure, we show the vector magnetogram (panel (e)) and the field lines (panel (f)) in the same, but a little larger subregion outlined by the black rectangle in panel (c). The vector magnetogram and field lines reveal that underlying the flare region is a bald patch (BP) located at the central portion of a long PIL (enhanced by the thick white line in panels (e) and (f)). By definition, a BP is a portion of the PIL with $(\mathbf{B} \cdot \nabla) B_z > 0$, which means that the horizontal field at the PIL crosses from negative to positive B_z (Titov et al. 1993; Bungey et al. 1996), which is the opposite of a normal case. In the middle of the BP, the transverse field is nearly parallel to the PIL, suggesting that it is not a single BP but fragments into two parts. The BPs can also be defined as the locations where the magnetic field is tangent to the photosphere, and the continuous set of field lines that graze the surface at the BP forms two separatrix surfaces that separate three different topological regions. The separatrix field lines are shown in Figure 7(f) and with 3D views in Figure 8. Several studies have demonstrated that the BP can be correlated to flares and even CMEs due to BP separatrices, in which strong current sheets can be formed by photospheric motions or flux emergence and trigger reconnection (e.g., Aulanier et al. 1998; Fletcher et al. 2001; Mandrini et al. 2002; Wang et al. 2002). The topological analysis of the flare site here thus suggests that the AR 11117 flare can also be interpreted as a *BP flare* (Aulanier et al. 1998; Delannée & Aulanier 1999) and may provide evidence in favor of reconnection along BP separatrices. The heights of the apexes of BP separatrices is about $2 \sim 3$ Mm, meaning that the flare happened rather low near the photosphere. However, in which way the current sheet was formed and how the reconnection was triggered are not clear, and an additional study relying on higher resolution and cadence data may be needed. For further evidence of the presence of the BP co-spatial with the flare, a curved dark feature near the flare location, shown by the arrows on the AIA image (see panel (a) of Figure 7), has the same shape with the field lines near the right end of the BP (indicated by the arrows in panel (f)). This can be explained well by the dip of field lines just above the BP, which can support dense cold plasma against gravity in the same way as filaments.

4.3. Energy and Current

In order to quantify the change of the field in the time series, we computed a set of parameters and summarized them in Table 1. They include the total unsigned magnetic flux $|\Phi|_{\rm tot} = \int_S |B_z|\, dS$ (where S represents the photosphere), the total unsigned current $|I|_{\rm tot} = \int_S |j_z|\, dS$ (i.e., the integral of the unsigned vertical current in the photosphere), the total energy $E_{\rm tot} = (1/8\pi) \int_V B^2 dV$, the potential energy $E_{\rm pot}$, the free energy $E_{\rm free} = E_{\rm tot} - E_{\rm pot}$, and the ratio of free energy to potential energy. All these parameters are important to characterize the evolution of the coronal magnetic field. The first four parameters, i.e., the magnetic flux, the current, the total, and the potential energies, all keep increasing with time in spite of the small flares. This is due to the fact that the energy

[4] Here, we need not to distinguish the footpoints of the positive and negative polarities, since Q is designed with the same value at conjugate footpoints of the same field line (Titov et al. 2002).

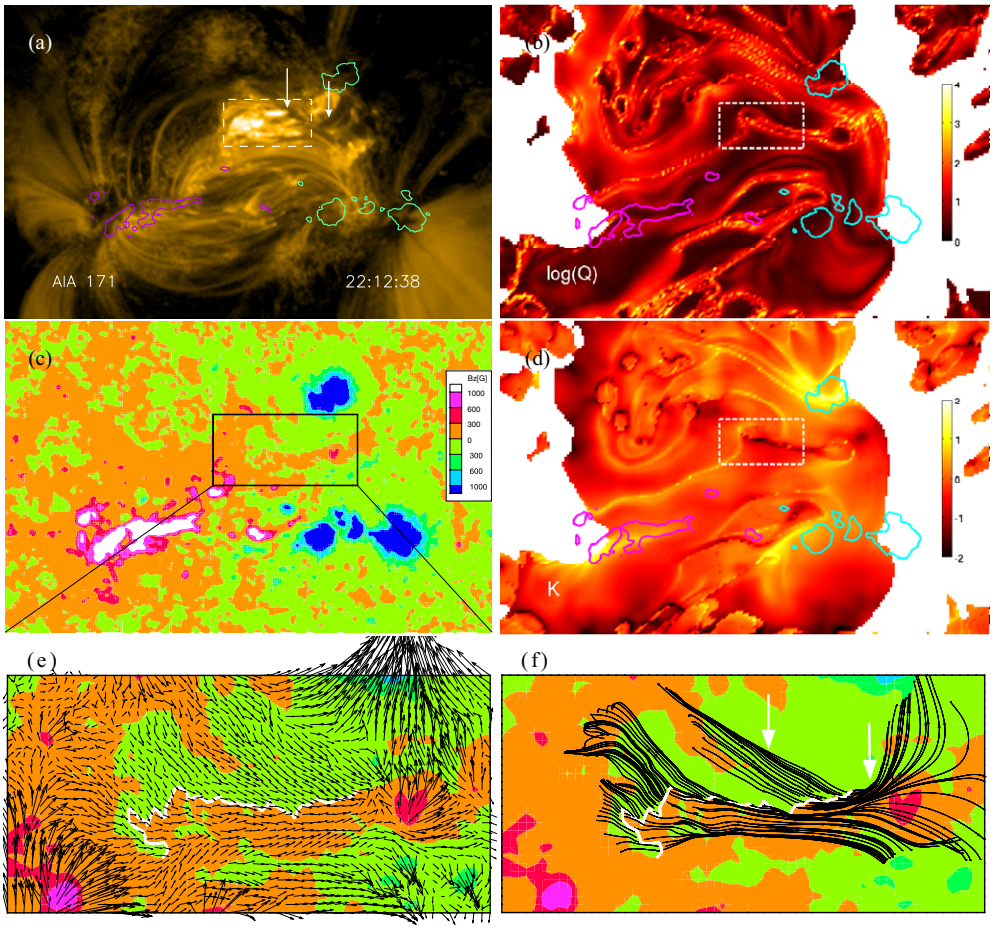

Figure 7. (a) The AIA 171 image at 22:12, with the contour lines plotted for the LoS photospheric field at ±1000 G and the dashed box showing the location of the flare with brightened loops. (b) The squashing factor Q in logarithmic scale; the same contours are plotted at ±1000 G for photospheric B_z and the dashed box outlines the flare location. (c) The B_z map with the flare location outlined by a black box enlarged in panel (e). (d) Same as (b) but for the expansion-contraction degree K. (e) The vector magnetogram in the flare location, and the thick white line denotes the bald patch (BP). Panel (f) gives some examples of the field lines (i.e., the BP separatrix field lines) that are tangent to the photosphere of the BP (the thick white line).

(A color version of this figure is available in the online journal.)

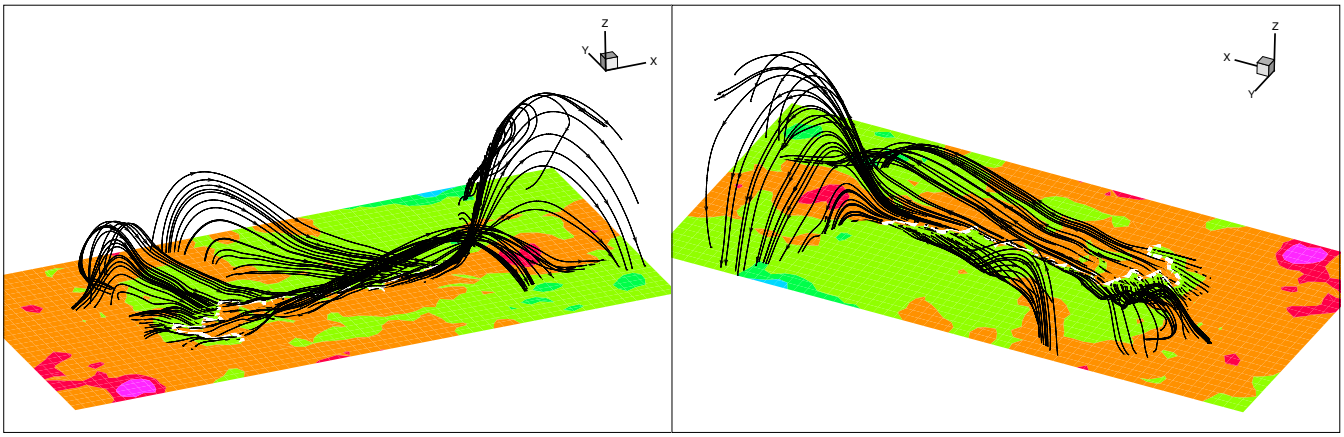

Figure 8. Different 3D views of the BP-separatrix field lines plotted in panel (f) of Figure 7. The BP is denoted by the thick white lines. The z-axis scale is doubled for a better view of the field lines.

(A color version of this figure is available in the online journal.)

injected by emerging magnetic flux is larger than the energy released by the flares (e.g., Régnier et al. 2005; He et al. 2011). The total energy and the potential energy are on the order of 10^{32} erg, which is the typical energy content of a medium-sized active region. Because of the non-potentiality of the field, the total energy $E_{\rm tot}$ is always higher than that of the potential field, which holds an energy minimum state with a given magnetic flux on the photosphere. It is commonly believed that free magnetic energy plays a fundamental role in flares, because the source of the energy for the flare must be magnetic and only a fraction

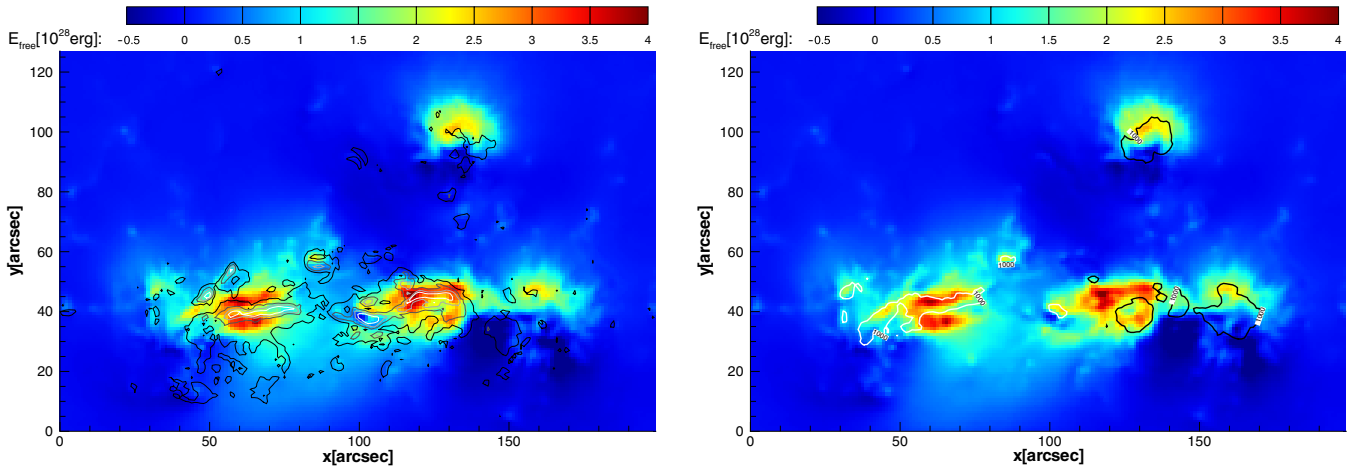

Figure 9. Images represent the vertical integral of free energy, showing the locations of free energy storage. The contour lines in the left panel represent the vertically integrated current density $\int |\mathbf{J}|\, dz$, and the lines are color-coded with the strength of the integrated current (increasing from black to white). The contour lines in the right panel represent B_z on the photosphere with a value of ± 1000 G.

(A color version of this figure is available in the online journal.)

Table 1
Variation of Parameters with Evolution of the Field

Time	$\|\Phi\|_{\rm tot}$ (10^{22} Mx)	$\|I\|_{\rm tot}$ (10^{13} A)	$E_{\rm tot}$ (10^{32} erg)	$E_{\rm pot}$ (10^{32} erg)	$E_{\rm free}$ (10^{31} erg)	$E_{\rm free}/E_{\rm pot}$	$e_{\rm m}$
21:00	1.60	4.77	4.80	4.04	7.66	0.19	0.00
21:36	1.63	4.80	4.95	4.18	7.69	0.18	0.09
22:00	1.65	4.84	5.05	4.27	7.78	0.18	0.11
22:12	1.66	4.92	5.09	4.33	7.61	0.18	0.10
22:36	1.68	4.96	5.21	4.41	7.95	0.18	0.11
23:00	1.70	5.05	5.28	4.50	7.79	0.17	0.13

Note. See the text for details.

of the total magnetic energy, i.e., free energy, can be converted to kinetic energy and flare radiation (Priest & Forbes 2002). Our computation shows that free energy is on the order of 10^{31} erg (close to 10^{32} erg), which seems to be sufficient to power a moderate flare, and this energy initially increased like the total and potential energies before the C-class flare started at 22:06 UT. One should bear in mind that even free energy is only partially involved with flares since the field after flares is still non-potential and nonlinear (e.g., see Schrijver 2009). The energy released by the flare ought to be quantified by the change in free energy from immediately before to after the flare. Although the total energy increased even in the interval of the flare, the free energy dropped as expected at 22:12, i.e., the peak time of the flare, with a small amount of about 1.7×10^{30} erg. It has been estimated that for the largest flares up to X-class, the energy released is on the order of 10^{32} erg (e.g., Priest 1981, 1987). Thus, by a rough estimation, the decrease in free energy of pre- and post-flares is actually adequate to power this minor flare, of which the energy needed is about several percent of the largest class. Nevertheless, caution is needed when estimating the energy budget of the flare by the drop in free energy in our modeling, since many aspects of the model and the specific approach may influence the results. We will discuss this in the conclusion. In the last column of Table 1, we calculated a mean vector deviation between field **b** at each time with respect to the field **B** at 21:00:

$$e_{\rm m} = \frac{1}{M} \sum_i \frac{|\mathbf{b}_i - \mathbf{B}_i|}{|\mathbf{B}_i|}, \tag{5}$$

where i denotes the indices of all the pixels of the computational volume and M is the total number of the pixels. As a metric monitoring the numerical variation of the field with the time, the very low values of $e_{\rm m}$ again show that the change of the field is rather small.

In addition to the global energy content, we can also study the spatial distribution of the magnetic free energy, i.e., the locations of the free energy storage. As an example, for the magnetic field at 22:00, we computed the vertical integration of the free energy

$$E_{\rm free}(x, y) = A \int \frac{\mathbf{B}^2 - \mathbf{B}_{\rm pot}^2}{8\pi}\, dz, \tag{6}$$

where $A = dx\, dy$, and plotted the distribution of $E_{\rm free}(x, y)$ on the horizontal plane (Figure 9). A sum of the energy $E_{\rm free}(x, y)$ in the images gives the total free energy listed in Table 1. In the left image of Figure 9, the contour lines show the vertically integrated current density $\int |\mathbf{J}|\, dz$, and the lines are color-coded with the strength of the integrated current (increasing from black to white); in the image on the right, the strongest regions of B_z in the photospheric field are outlined by the contour lines (± 1000 G). It can be clearly seen that the distribution of free energy is largely co-spatial with that of the current. This can be easily understood because coronal free energy (or the non-potential energy) is actually stored in the current-carrying field (where non-potentiality is strong). On the other hand, as shown by the image on the right, the concentrations of free energy are not generally spatially correlated with those of the strongest magnetic flux. It should be noted that in the image, there are some places with negative values of vertically integrated free

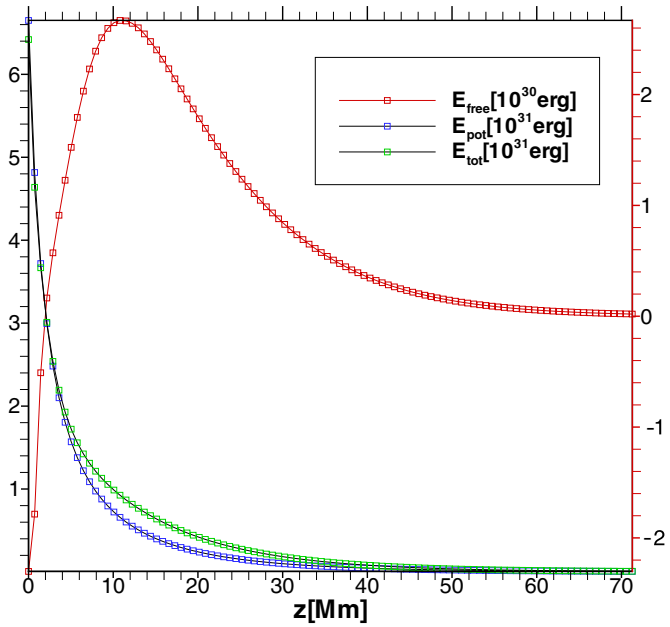

Figure 10. Variation of the horizontal surface integration of magnetic field energy along the z-axis. Note that the left vertical axis (black) indicates values for $E_{\rm pot}$ and $E_{\rm tot}$, and the right vertical axis (red) indicates values for $E_{\rm free}$.
(A color version of this figure is available in the online journal.)

energy. This is physically valid since there is no restriction that the energy density (and thus any sub-volume energy) must always be greater than that of the potential field, although a non-potential field must have a global energy content greater than the potential field (e.g., Mackay et al. 2011). In Figure 10, we plot the horizontal surface integral of the total energy, the potential energy, and the free energy, e.g.,

$$E_{\rm free}(z) = \int dz \int \frac{\mathbf{B}^2 - \mathbf{B}_{\rm pot}^2}{8\pi}\, dx\, dy, \qquad (7)$$

as functions of the height z. The total and the potential energies are predominantly located near the photosphere where the magnetic field strength is high, whereas the free energy (the red curve) is situated mainly above the photosphere in a range of 5 Mm to 30 Mm with its maximum at about 10 Mm. It is interesting to find that near the photosphere, the free energy is negative with a minimum value at the photosphere, which means that the observed vector field has a lower surface energy content than the potential field. This is, however, not surprising as we have noted that any sub-volume energy content of the non-potential field may be lower than the potential energy.

An electric current can characterize the non-potentiality of the field, e.g., the patterns of a strong current concentration may serve as a proxy for non-potential structures (e.g., the sigmoids) in the corona (Schrijver et al. 2008; Archontis et al. 2009; Sun et al. 2012). In particular, the current structures are regions where reconnection may happen and magnetic energy is converted to thermal energy and heat, thus creating hot emission. In Figure 11, we give examples of synthetic images of the current, which is computed by the vertical integration of J^2 (i.e., $\int_z J^2\, dz$; see Archontis et al. 2009), and compared to the AIA 304 Å images. Since the term J^2 is proportional to

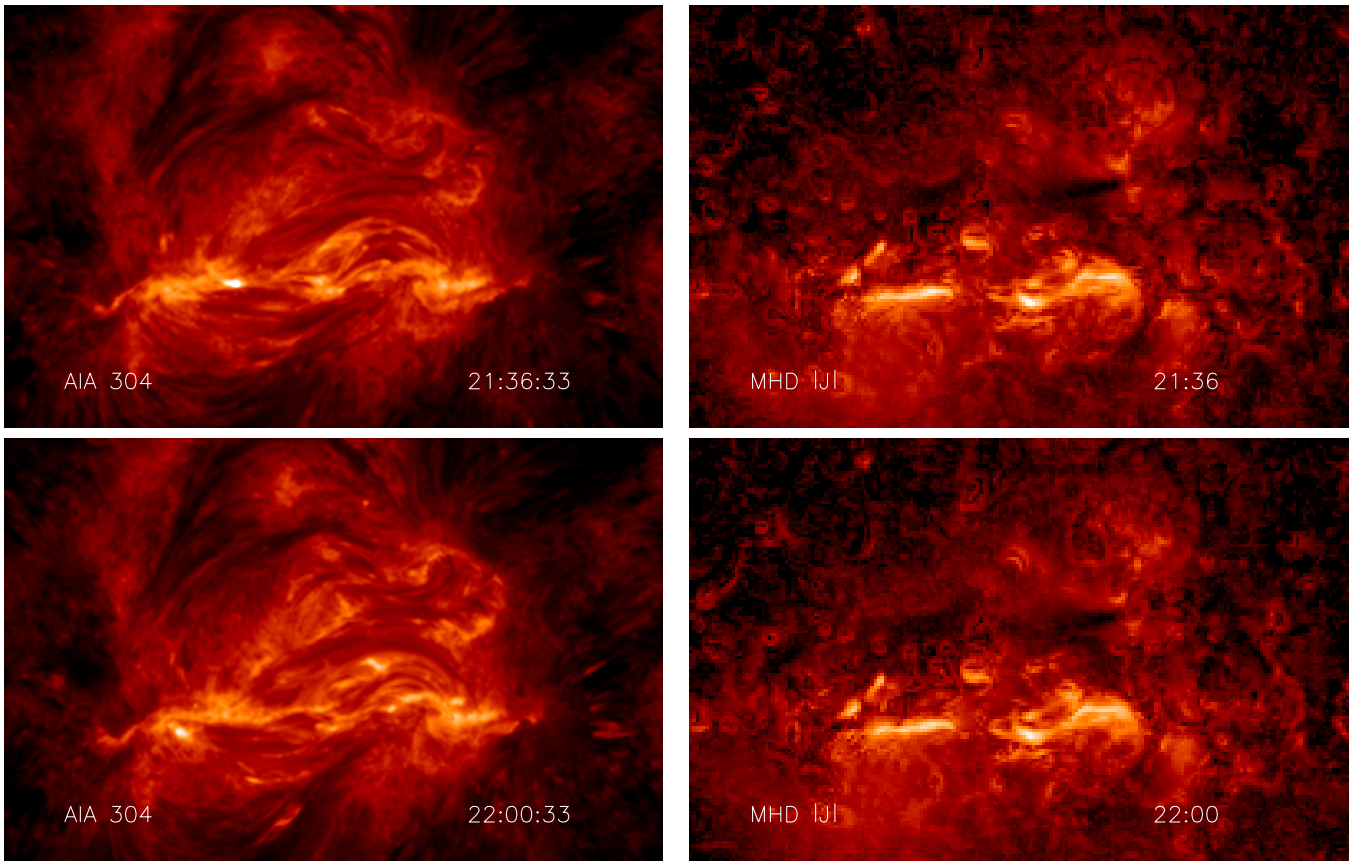

Figure 11. Left column is the AIA 304 Å image and the right column is the synthetic images of a current using the vertical integral of J^2 computed by the MHD model.
(A color version of this figure is available in the online journal.)

the Joule heating term, it thus but very roughly simulates the hot emission. As can be seen in the figure, the strong current regions are indeed coincident to the regions with a high intensity of emission. However, the result does not show any intensive current associated with the flare site. This may be because the current sheet in the BP separatrices is very thin and has failed to be resolved by the present grid resolution.

5. CONCLUSIONS

In this work, we have applied the data-driven CESE–MHD model to investigate the 3D magnetic field of AR 11117 around the time of a C-class confined flare that occurred on 2010 October 25. Similar to the field extrapolation method, our model is designed to focus on the magnetic field, but its nonlinear dynamic interactions with plasma and finite gas pressure (denoted by plasma β) are also embedded, although they are simplified. Assuming that the dynamic evolution of the coronal magnetic field can be approximated by successive equilibria, we have solved a time sequence of MHD equilibria based on a set of vector magnetograms for AR 11117 taken by *SDO*/HMI around the time of the flare. By analyzing the computed 3D magnetic field along with the observation, we have the following results.

1. The model has qualitatively reproduced the basic structures of the magnetic field as supported by the visual similarity between the field lines and the *SDO*/AIA loops, which shows that the coronal field can indeed be well characterized by the MHD equilibrium in most times. The magnetic field is very non-potential with a strong local shear and some twists compared to the potential model. There are also some loops that failed to be recovered by the MHD model, but only at a time set very close to the flare. This means that the magnetic field is rather dynamic when energy is suddenly released in a timescale far shorter than that of relaxation by Alfvén speed.
2. The magnetic configuration changes are very limited during the studied time interval of 2 hr, and the flare-related reconnection takes place on a rather small scale and at a low height near the photosphere. Topological analysis reveals that the small flare is correlated with a BP and the energy dissipation can be understood by the reconnection associated with the BP separatrices. However, no intensive current is found in the flare site related to the BP separatrices. This may be because the current sheet associated with the separatrices is very thin and cannot be resolved by the present grid resolution. Further study exploiting full resolution and high-cadence observations is required to explain how the BP flare is activated, e.g., where the current sheet is formed and how the reconnection is triggered.
3. Because of continuous flux emergence, the total unsigned magnetic flux and the current through the photosphere keep increasing (but very slightly) in spite of the flare. Although evolution of the total magnetic energy also exhibits the same tendency as that of the total magnetic flux, the sum of free energy for the computational volume drops when the flare occurred, indicating that some of the non-potential energy is released by the flare. Our computation shows that the amount of free energy loss is on the order of 10^{30} erg, which is adequate to power a minor C-class flare.

In summary, our model captures the basic features of the 3D magnetic field of the target active region both qualitatively and quantitatively, and the results give some hints to the trigger mechanism of the flare. Nevertheless, we remind readers that the results, especially in the quantitative aspect, should be interpreted with caution because they can be influenced by many uncertainties in the modeling. The uncertainties also exist in other similar models for example, the NLFF modeling. Even for this model, different codes may produce very inconsistent results (Schrijver et al. 2008; DeRosa et al. 2009). The uncertainties may first come from a measurement error of the HMI magnetogram data. For example, Sun et al. (2012) have estimated that the free energy content could be affected by the spectropolarimetric noise in the magnetogram by several percent; even such a small error is large for the present case in which the flare may only release a very small fraction of free energy. It should be noted that in the NLFF model, systematic error can be greater because of the force-free assumption and the preprocessing and smoothing of the original data. Although our model does not suffer from such a preprocessed-related problem, systematic uncertainties can still come from the simplified configuration of the solar atmosphere, the boundary conditions, and the data interpolation from the original non-uniform grid to a uniform grid when computing the parameters. The use of a low-β plasma globally is especially far from the realistic case in which the solar atmosphere is highly stratified with much more gas pressure near the photosphere. Furthermore, the assumption of a static state of the magnetic field is unjustified by the onset of the flare, which can make the field lines very dynamic and our computation unreliable, as discussed in the comparison of the MHD results with the AIA images. This is a much more basic problem (than the others aforementioned) encountered by any extrapolation of the magnetic field with static or quasi-static models.

Future improvements should be made in several aspects. To increase the capability of adaptive resolving, the small-scale structures can hopefully be realized by the aid of the adaptive-mesh-refinement technique. Exploiting more observations, like the surface flows computed by the LCT-type methods, can further constrain the model and provide important information for the realistic dynamic evolution of the magnetic field. A more physics-based thermodynamic model for the solar atmosphere with a stratified temperature will also be considered to couple the photosphere and corona, in order to model the behavior of the magnetic field in a highly stratified and inhomogeneous plasma with β from >1 to $\ll 1$.

This work is jointly supported by the 973 program under grant 2012CB825601, the Chinese Academy of Sciences (KZZD-EW-01-4), the National Natural Science Foundation of China (41031066, 40921063, 40890162, and 41074122), and the Specialized Research Fund for State Key Laboratories. Data are courtesy of NASA/*SDO* and the AIA and HMI science teams. Special thanks to our anonymous reviewer for valuable suggestions that helped improve the paper.

REFERENCES

Abbett, W. P. 2007, ApJ, 665, 1469
Abbett, W. P., Mikić, Z., Linker, J. A., et al. 2004, J. Atmos. Sol.-Terr. Phys., 66, 1257
Amari, T., Boulmezaoud, T. Z., & Aly, J. J. 2006, A&A, 446, 691
Antiochos, S. K. 1987, ApJ, 312, 886
Archontis, V., Hood, A. W., Savcheva, A., Golub, L., & Deluca, E. 2009, ApJ, 691, 1276
Aschwanden, M. J. 2011, Living Rev. Sol. Phys., 8, 5
Aulanier, G., Démoulin, P., Schmieder, B., Fang, C., & Tang, Y. H. 1998, Sol. Phys., 183, 369

Bungey, T. N., Titov, V. S., & Priest, E. R. 1996, A&A, 308, 233
Canou, A., & Amari, T. 2010, ApJ, 715, 1566
Chae, J. 2001, ApJ, 560, L95
Delannée, C., & Aulanier, G. 1999, Sol. Phys., 190, 107
Demoulin, P., Bagala, L. G., Mandrini, C. H., Henoux, J. C., & Rovira, M. G. 1997, A&A, 325, 305
Demoulin, P., Henoux, J. C., Priest, E. R., & Mandrini, C. H. 1996, A&A, 308, 643
Démoulin, P., & Pariat, E. 2009, Adv. Space Res., 43, 1013
DeRosa, M. L., Schrijver, C. J., Barnes, G., et al. 2009, ApJ, 696, 1780
Fan, Y. L., Wang, H. N., He, H., & Zhu, X. S. 2011, ApJ, 737, 39
Fan, Y.-L., Wang, H.-N., He, H., & Zhu, X.-S. 2012, Res. Astron. Astrophys., 12, 563
Fang, F., Manchester, W., Abbett, W. P., & van der Holst, B. 2010, ApJ, 714, 1649
Feng, X., Hu, Y., & Wei, F. 2006, Sol. Phys., 235, 235
Feng, X., Zhou, Y., & Wu, S. T. 2007, ApJ, 655, 1110
Fletcher, L., López Fuentes, M. C., Mandrini, C. H., et al. 2001, Sol. Phys., 203, 255
Guo, Y., Ding, M. D., Wiegelmann, T., & Li, H. 2008, ApJ, 679, 1629
He, H., Wang, H., & Yan, Y. 2011, J. Geophys. Res., 116, 1101
Jiang, C., Feng, X., Fan, Y., & Xiang, C. 2011, ApJ, 727, 101
Jiang, C. W., & Feng, X. S. 2012, ApJ, 749, 135
Jiang, C. W., Feng, X. S., Zhang, J., & Zhong, D. K. 2010, Sol. Phys., 267, 463
Jing, J., Tan, C., Yuan, Y., et al. 2010, ApJ, 713, 440
Lin, H., Kuhn, J. R., & Coulter, R. 2004, ApJ, 613, L177
Longcope, D. W. 2005, Living Rev. Sol. Phys., 2, 7
Low, B. C., & Lou, Y. Q. 1990, ApJ, 352, 343
Mackay, D. H., Green, L. M., & van Ballegooijen, A. 2011, ApJ, 729, 97
Mandrini, C. H., Demoulin, P., Rovira, M. G., de La Beaujardiere, J.-F., & Henoux, J. C. 1995, A&A, 303, 927
Mandrini, C. H., Démoulin, P., Schmieder, B., Deng, Y. Y., & Rudawy, P. 2002, A&A, 391, 317
Metcalf, T. R., DeRosa, M. L., Schrijver, C. J., et al. 2008, Sol. Phys., 247, 269
Metcalf, T. R., Jiao, L., McClymont, A. N., Canfield, R. C., & Uitenbroek, H. 1995, ApJ, 439, 474
Mikic, Z., & Linker, J. A. 1994, ApJ, 430, 898
Nakagawa, Y. 1981, ApJ, 247, 707
Priest, E. R. 1981, Solar Flare Magnetohydrodynamics (London: Gordon and Breach)
Priest, E. R. (ed.) 1987, Solar Magneto-hydrodynamics (Dordrecht: Reidel)
Priest, E. R., & Démoulin, P. 1995, J. Geophys. Res., 100, 23443
Priest, E. R., & Forbes, T. G. 2002, A&AR, 10, 313
Régnier, S., & Canfield, R. C. 2006, A&A, 451, 319
Régnier, S., Fleck, B., Abramenko, V., & Zhang, H. 2005, in Chromospheric and Coronal Magnetic Fields, Vol. 596, ed. D. E. Innes, A. Lagg, & S. K. Solanki (Noordwijk: ESA), 61
Schrijver, C. J. 2009, Adv. Space Res., 43, 739
Schrijver, C. J., DeRosa, M. L., Metcalf, T., et al. 2008, ApJ, 675, 1637
Seehafer, N. 1994, A&A, 284, 593
Shibata, K., & Magara, T. 2011, Living Rev. Sol. Phys., 8, 6
Solanki, S. K., Inhester, B., & Schüssler, M. 2006, Rep. Prog. Phys., 69, 563
Solanki, S. K., Lagg, A., Woch, J., Krupp, N., & Collados, M. 2003, Nature, 425, 692
Sun, X., Hoeksema, J. T., Liu, Y., et al. 2012, ApJ, 748, 77
Sun, X., Hoeksema, J. T., Wiegelmann, T., Hayashi, K., & Liu, Y. 2010, AGU Fall Meeting Abstracts (San Francisco, CA: AGU), A1607
Tadesse, T., Wiegelmann, T., Inhester, B., & Pevtsov, A. 2012, Sol. Phys., 60
Thalmann, J. K., & Wiegelmann, T. 2008, A&A, 484, 495
Titov, V. S., & Démoulin, P. 1999, A&A, 351, 707
Titov, V. S., Hornig, G., & Démoulin, P. 2002, J. Geophys. Res., 107, 1164
Titov, V. S., Priest, E. R., & Demoulin, P. 1993, A&A, 276, 564
Valori, G., Green, L. M., Démoulin, P., et al. 2012, Sol. Phys., 278, 73
Valori, G., Kliem, B., & Fuhrmann, M. 2007, Sol. Phys., 245, 263
Wang, A. H., Wu, S. T., Liu, Y., & Hathaway, D. 2008, ApJ, 674, L57
Wang, T., Yan, Y., Wang, J., Kurokawa, H., & Shibata, K. 2002, ApJ, 572, 580
Welsch, B. T., Fisher, G. H., Abbett, W. P., & Regnier, S. 2004, ApJ, 610, 1148
Wheatland, M. S., Sturrock, P. A., & Roumeliotis, G. 2000, ApJ, 540, 1150
Wiegelmann, T. 2004, Sol. Phys., 219, 87
Wiegelmann, T. 2008, J. Geophys. Res., 113, 3
Wiegelmann, T., Inhester, B., & Sakurai, T. 2006, Sol. Phys., 233, 215
Wiegelmann, T., Thalmann, J. K., Inhester, B., et al. 2012, Sol. Phys., 67
Wu, S. T., & Wang, J. F. 1987, Comput. Methods Appl. Mech. Eng., 64, 267
Wu, S. T., Wang, A. H., Gary, G. A., et al. 2009, Adv. Space Res., 44, 46
Wu, S. T., Wang, A. H., Liu, Y., & Hoeksema, J. T. 2006, ApJ, 652, 800